Wet roots of high elevation in the western United States

Michael A. Berry[1], Anthony R. Lowry[2], Xiaofei Ma[2,3], Ravi V.S. Kanda[2], Derek L. Schutt[4]

1- *Now at ConocoPhillips Alaska, Anchorage, AK*
2- *Utah State University, Department of Geosciences, Logan, UT*
3- *Now at Los Alamos National Laboratory, EES-17, Los Alamos, NM*
4- *Colorado State University, Department of Geosciences, Fort Collins, CO*

Highlights

• Cordilleran Moho temperatures are lower than predicted from surface heat flow
• The difference implicates melt and volatile thermodynamics and transport
• Thermal anomalies correlate to elevation from crustal and asthenospheric buoyancy
• Hydration reaction heating of subduction wedges may dominate Cordilleran elevation

Abstract

Lithospheric heat transfer strongly modulates the distributions of melt, rock strength, and buoyancy that are responsible for volcanism, seismicity, and elevation. Geotherm models often extrapolate shallow (< 3 km) heat flow measurements but are complicated by near-surface hydrology, poorly-known crustal thermal properties, and deep advective transfer by melts and volatiles. Here we compare temperatures estimated from P-wave velocities in the uppermost mantle to those modeled from surface heat flow in the western United States. We show that U.S. Cordilleran regions of high heat flow and high elevation have deep temperatures much lower than predicted by steady-state conductive cooling models. We hypothesize that the discrepancy reflects reaction thermodynamics and advection by migration of volatiles and melts up the lithospheric column. Hydration of the mantle and lower crust by Farallon subduction consumes garnet into melts that absorb latent heat in the lower crust and upper mantle, while hydration reaction enthalpy heats the subduction back-arc mantle, and advection amplifies surface heat flow. This process would increase elevation both by raising temperatures and by converting dense constituents of the mineral assemblage to more buoyant intrusions in the middle and upper crust. The results imply hydration reaction enthalpy changes play a significant role in the dynamics of Cordilleran regions.

1. Introduction

The sources of high elevation in Cordilleran regions have long been enigmatic, but offsetting buoyancy from thin crust and warm lithosphere require a large role for asthenospheric buoyancy in subduction back-arc mobile belts (Lowry et al., 2000; Becker et al., 2014). High surface heat flow and low mantle shear velocities support an inference of hot asthenospheric wedge material in subduction back-arcs (Hyndman et al., 2005), but these observations are puzzling given that heat transfer to the subducting slab should refrigerate the overlying mantle, leading some to postulate an (equally puzzling) anomalously hot source for wedge flow (Currie and Hyndman, 2006; Zhou et al., 2018).
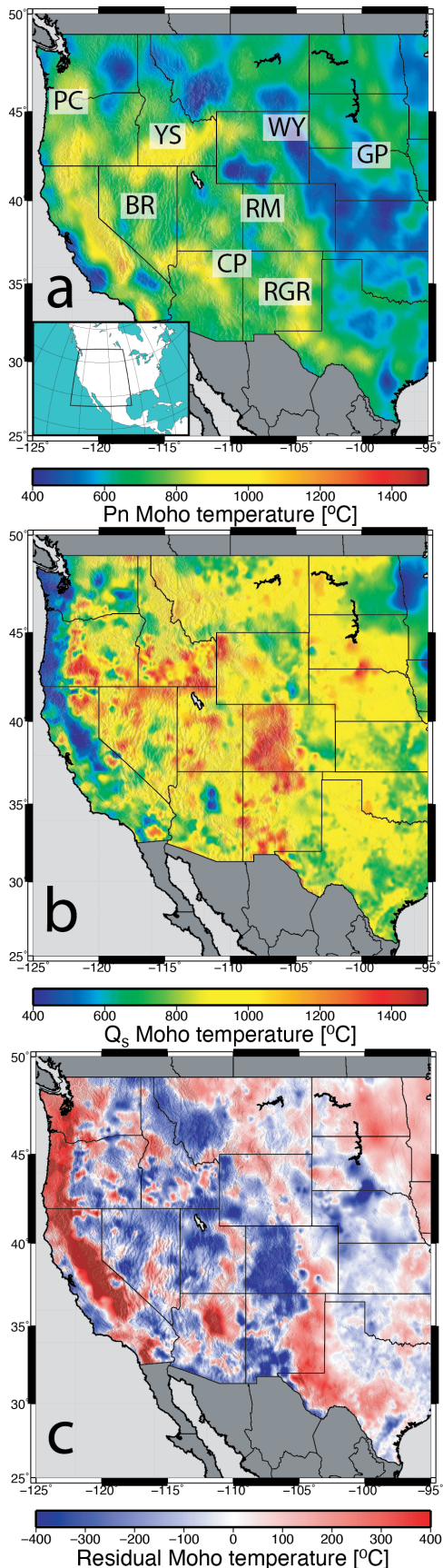
Figure 1. Upper mantle temperature models. a, Pn-derived Moho temperature. Labels are: PC: Pacific coast, YS: Yellowstone hotspot track, BR: Basin and Range, RM: Rocky Mountains, CP: Colorado Plateau, RGR: Rio Grande rift, WY: Wyoming high-plains, GP: Great Plains. **b**, Moho temperature modeled from surface heat flow. **c**, Residual (a minus b).

Knowledge of Earth's thermal structure is crucial to understanding tectonics, elevation, seismicity, and magmatism. Extrapolations of shallow (< 3 km) borehole measurements of heat flow to the deeper lithosphere (Pollack and Chapman, 1977; Artemieva and Mooney, 2001) remain an important constraint on temperatures, but continental heat flow is complicated by near-surface hydrology, crustal heat production, and tectono-magmatic history (Furlong and Chapman, 2013). Ambiguities in continental expressions of crustal heat production and tectono-magmatism require remote-sensed in-situ estimates of temperature to resolve. Moho temperature estimates from mineral physics of P-wave velocities in the uppermost mantle (using the refracted Pn phase) minimize errors in both temperature (~50–120 °C) and depth (~5 km) (Schutt et al., 2018). Western U.S. Moho temperatures (Fig. 1a) mostly fall in the range from 440 to 900 °C. Here we examine differences in seismically-derived Moho temperature estimates (Schutt et al., 2018) and predictions by conductive thermal models of surface heat flow, as well as their possible implications for buoyancy in Cordilleran back-arc regions.

2. Methods

2.1. Observational constraints

To facilitate comparison of Pn-derived Moho temperature estimates (Fig. 1a) to surface heat flow, Q_s (Fig. 2a), we model a predicted Moho temperature (Fig. 1b) assuming one dimensional conductive heat transfer. Conductive geotherm modeling depends on surface temperature, mantle asthenospheric temperature, crustal thickness, heat production by decay of radioactive elements, and rock thermal conductivity. Several of these fields vary only laterally and can be constrained directly from measurements. We affix surface temperatures, T_S, to means from a climatological data product (Grieser et al., 2006) (Fig.
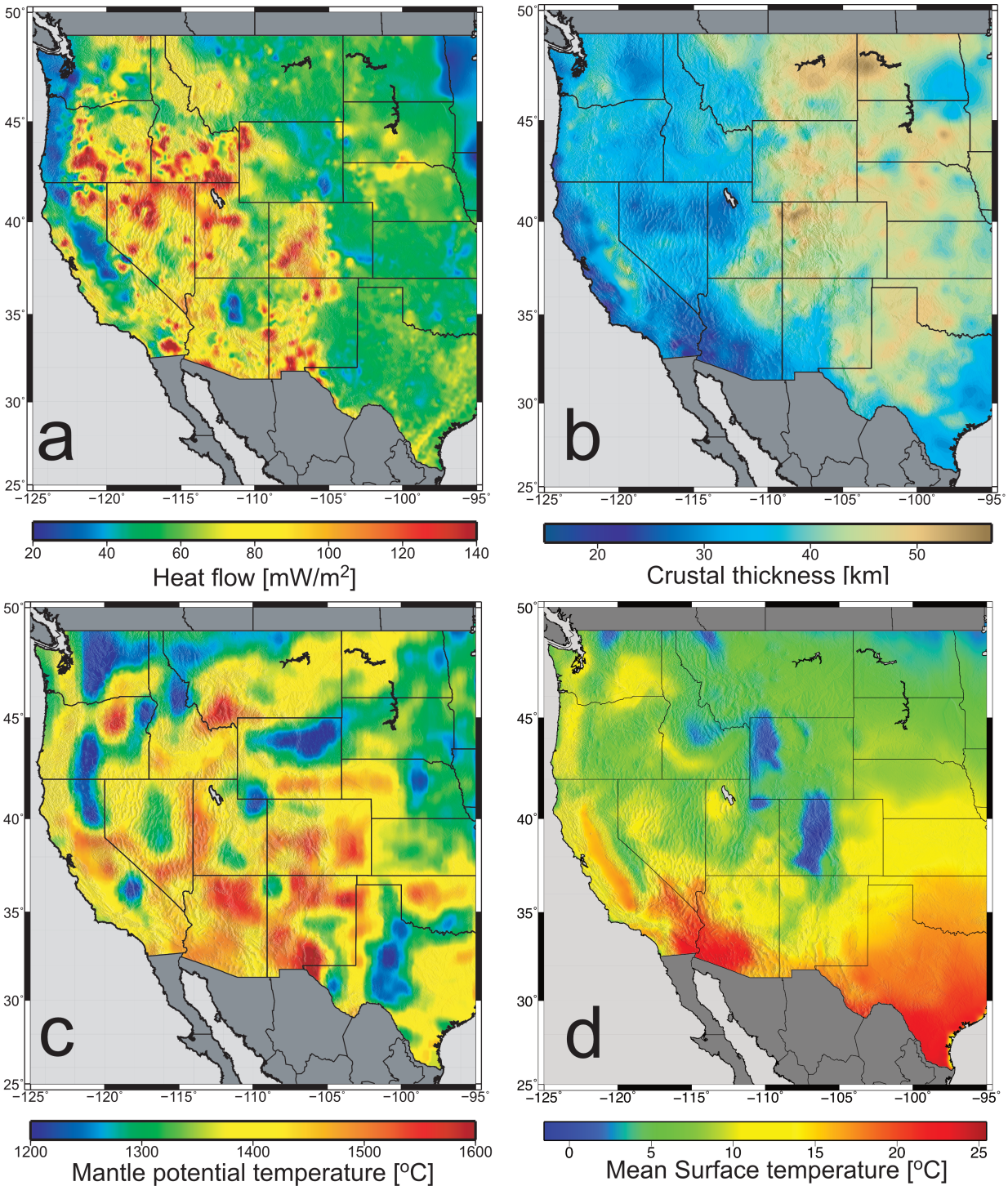
Figure 2. **Fields for thermal modeling of surface heat flow. a**, Surface heat flow from filtered borehole and bottom-hole temperature measurements. **b**, Crustal thickness. **c**, Mantle potential temperature from deep shear velocities. **d**, Mean surface temperature.

2d), and estimate asthenospheric mantle potential temperatures, T_m (Fig. 2c), from mineral physics mapping (Cammarano et al., 2003) of shear-wave tomography at 230 km (Schmandt and Lin,

2014). The deep potential temperature estimates have larger uncertainties than Pn-derived Moho temperature, but plausible alternative approaches have negligible impact upon our conclusions (Supplementary Material). Geotherms are modeled to match optimally-interpolated surface heat flow measurements from a combined database of borehole and industry bottom hole temperature measurements (Fig. 2a) (Blackwell et al., 2007).

Borehole temperature data are unevenly distributed over the study area (Supplemental Fig. S5). Dense measurements include bottom hole temperatures from regions with high oil and gas production (primarily in the Great Plains regions in the eastern part of our study area). Heat flow in other regions is sampled more sparsely by borehole temperature profiles. Nevertheless, heat flow in the western United States is sampled much more densely than any other similar-sized region of the world, affording high confidence in the significance of results that are averaged on ~100 km scales. Measurements in the eastern U.S. are not as dense and are excluded from this study.

Surface heat flow measurements are often perturbed by topographic and near-surface groundwater effects (Gosnold, 1985), so we filter the interpolated heat flow using the approach described by Mareschal et al. (1985) to remove anomalies that would require a source or sink above 35 km depth. Despite attempts to mitigate near-surface effects, some are sufficiently widespread that they remain, with one example being extremely low heat flow in the southern Colorado Plateau (Morgan et al., 2010). Heat-flow-derived geotherms are sampled at a depth three km below the Moho (Fig. 2b) estimated from a joint inversion of USArray seismic receiver functions and gravity (Ma & Lowry, 2017; Lowry & Pérez-Gussinyé, 2011), corresponding to the mean depth of Fresnel zone sampling by the Pn product (Buehler and Shearer, 2017), prior to comparison with the Pn-derived Moho temperature product.

2.2. Geotherm modeling

Assessing whether thermal transfer is better described by steady-state or time-dependent (cooling) physics is an important first step in conductive thermal modeling of the lithosphere (e.g., Furlong & Chapman, 2013). The most common approach to approximating thickness of the continental thermal boundary layer proscribes a depth at which a geotherm intersects the mantle adiabat, but this geothermal end-member implicitly assumes steady-state (time $t = \infty$) lithospheric transport of basal heat supplied by mantle convection, and predicts high end-member temperatures throughout the deep lithosphere (Fig. 3). Steady-state conduction is an appropriate choice for stable continental lithosphere, but western U.S. Cordilleran geotherms are perturbed by tectonism relatively recently, and (as we will show) the challenge for geothermal modeling lies in achieving temperatures cold enough to match seismic observations at the Moho over much of the region. Consequently, we model a low-temperature end-member (Fig. 3) error function representation of the geotherm (Lowry et al., 2000), $T(z) - T_S \propto (T_m - T_S)\,\mathrm{erf}\,(z/l_{con})$, where l_{con} is a conductive thermal length-scale. This formulation closely approximates the geotherm and heat flow when advection is related to steady-state lithospheric strain (Lowry et al., 2000) or when the geotherm is dominated by cooling.
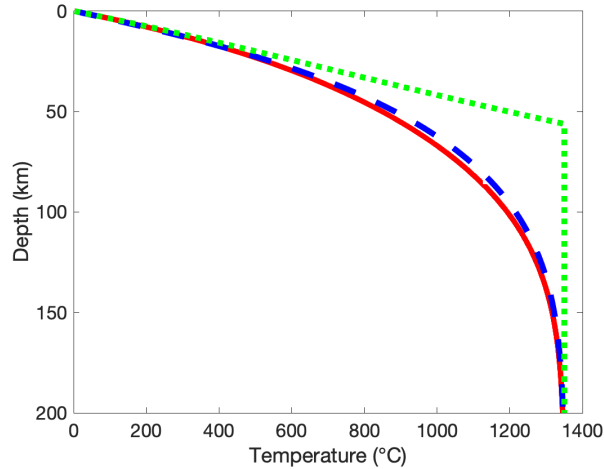
Figure 3. End-member physics for lithospheric geotherm modeling. Green dotted geotherm assumes steady-state transport of basal heat flow supplied by convection; red assumes half-space cooling. Blue dashed geotherm is a numerical cooling model; difference from the red curve illustrates error in the analytical approximation, equation (3). All assume identical surface heat flow, crustal radioactive heating, and temperature-dependent thermal conductivity.

After the physics of heat transfer, conductive geotherms are most sensitive to choices of rock thermal conductivity, k, and crustal radioactive heat production (Furlong and Chapman, 2013). Thermal conductivity is temperature-sensitive and has the empirical form $k = 1/(A + BT)$ (Siepold, 1998), where A and B depend on lithology (primarily, quartz-abundance). We infer an upward-concentrated depth distribution of radioactive elements (Turcotte and Oxburgh, 1972) characterized by an exponential decrease of heat production with depth:

$$A(z) = A_0 \exp\left(-{}^{z}\!/\!_{l_{rad}}\right) [\mu W\ m^{-3}], \tag{1}$$

in which A_0 is surface heat production and l_{rad} is a length-scale for decreasing concentration. Radioactive heat production in crustal rocks varies widely (e.g., Hasterok et al., 2018), but the total contribution must accord with measured heat flow via $Q_s = Q_r + Q_m$, in which Q_m is conductive heat flux from the convecting mantle and/or cooling, and Q_r is the integral of crustal radioactive heating:

$$Q_r = A_0 l_{rad}\left[1 - \exp\left(\frac{-h}{l_{rad}}\right)\right] \tag{2}$$

where h is crustal thickness (Fig. 2b).

Using the relations for conductive cooling, temperature-dependent thermal conductivity and depth-dependent radioactive heating above, temperature within the crust can be approximated analytically via the expression:

$$T(z) = T_S + \frac{AA_0 l_{rad}^2\left[1 - \exp\left(-\frac{z}{l_{rad}}\right) - \mathrm{erf}\left(\frac{z}{l_{con}}\right)\right] + (T_m - T_S)\mathrm{erf}\left(\frac{z}{l_{con}}\right)}{1 - BA_0 l_{rad}^2\left[1 - \exp\left(-\frac{z}{l_{rad}}\right) - \mathrm{erf}\left(\frac{z}{l_{con}}\right)\right]} \tag{3}$$

Evaluating the derivative of equation (3) at $z = 0$, the conductive thermal length parameter, l_{con}, relates directly to surface heat flow as:

$$l_{con} = \frac{2}{\sqrt{\pi}} \frac{\frac{T_m - T_S}{A + BT_S} - l_{rad}Q_r}{Q_s - Q_r} \tag{4}$$

The derivation of equation (3) assumes independence of the thermal conductivity and radioactive heating, which is not strictly correct. Temperature changes introduced by radioactive heating alter the thermal conductivity, which in turn affects the thermal gradient in a manner that
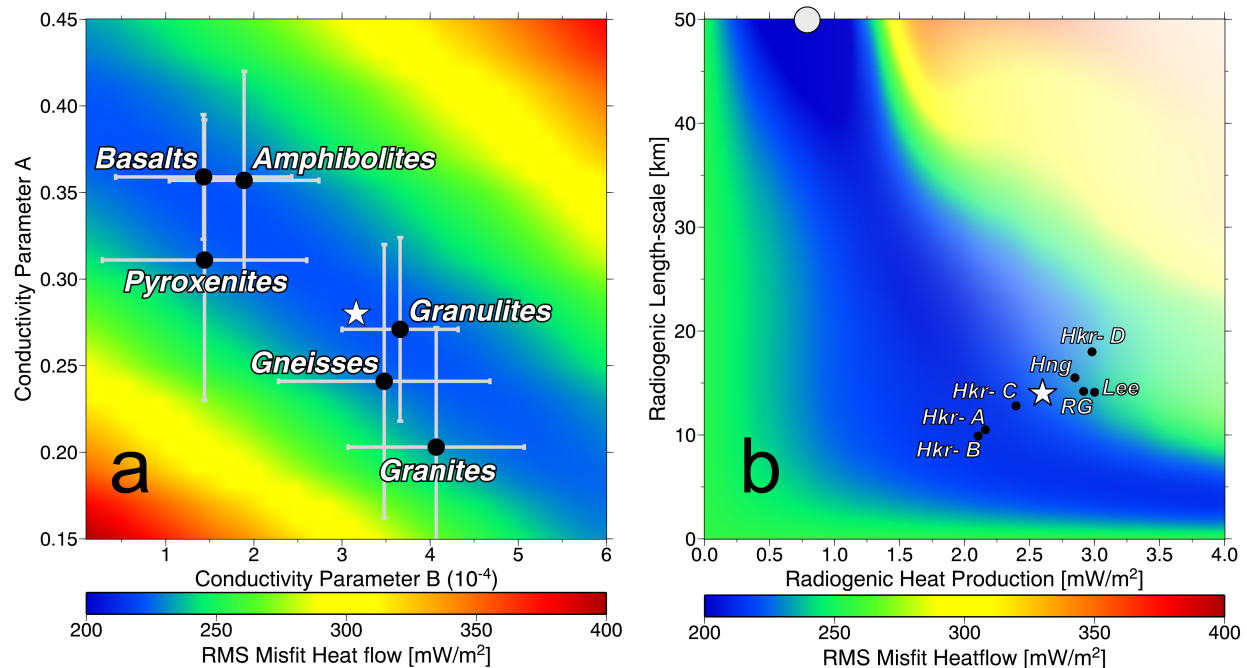
Figure 4. Thermal conduction and radioactive heating parameters. a, Dependence of RMS misfit of Moho temperatures on thermal conductivity parameters. White star is best-fit parameterization; black circles with 2σ variation are lab measurements. **b,** RMS misfit for crustal heating parameters. White star is parameterization used for this study. White circle is the best fitting parameterization; black circles are mean continental crustal compositions from petrologic models of Hacker et al., 2015 (Hkr: A through D); Huang et al., 2013 (Hng); Rudnick and Gao, 2003 (RG); and Lee et al., 2007 (Lee). Desaturation reflects fractional area of surface heat flow (Fig. 2a) less than the crustal heating model permits.

cannot be addressed without invoking numerical approximation. Fig. 3 illustrates a numerical solution for a cooling geotherm demonstrating that approximation using equation (3) underpredicts temperatures by up to a few tens of °C. However, the error is generally <10 °C at Moho depths (and the difference between numerical and analytical geotherms is dominated by numerical error if either B or A_0 is zero). This bias error is far smaller than other uncertainties, and computation of the Moho temperature with equation (3) is extremely efficient.

We examine a range of possible thermal conductivity parameters to assess their impact on misfit between Pn and heat flow estimates of Moho temperature in Fig. 4a. Root-mean square (RMS) misfit is minimized by parameters near the mean for laboratory measurements of crustal rocks (Siepold, 1998; Kukkonen et al., 1999). We examined other possible approaches, including conductivity parameters that vary according to seismically-imaged quartz abundance (SM), but these yielded negligible improvement. Consequently, the model shown in Fig. 1b assumes a uniform mean of measured crustal properties (white star).

RMS misfit of Moho temperatures for a range of parameterizations of uniform crustal heating is shown in Fig. 4b. Crustal heating for mean continental crustal composition models is also plotted in Fig. 4b, indicated by A_0 and l_{rad} parameters that most closely approximate the depth-dependence of heating in uniform layers for each petrologic model. RMS misfit between surface

heat flow and Pn estimates of Moho temperature is minimized by an extremal parameterization well outside the range of petrologic models of averaged continental crustal composition (white circle, see Fig. 4b and SM) and with a surface heat production value well below the mean of measurements from hand-samples and aerospectral gamma surveys. Consequently, the minimum-RMS misfit parameterization of crustal heating was rejected as implausible and a mean parameterization from the petrologic models was used (white star). Alternative parameterizations of uniform or spatially-varying heat production change our conclusions negligibly (SM), so the Q_s-derived model of Moho temperature in Fig. 1b uses the best-fitting uniform radioactive heating parameters represented by the star in Fig. 4b.

3. Results

Fig. 1c shows a residual discrepancy between the surface heat flow model and Pn-derived Moho temperature. Here, warmer colors (in red) indicate Moho that has higher temperature than predicted by surface heat flow. Much of the western Cordillera and a significant portion of the Great Plains exhibits a cooler Moho than surface heat flow would predict. If geotherms are parameterized correctly, any significant difference (i.e., exceeding the 50-120 °C uncertainties in the Schutt et al. (2018) temperature product) between upper mantle Pn temperature estimates and the surface heat flow model of Moho temperature implies a (transient) violation of the steady-state and/or conductive physics assumed by the geotherm model.
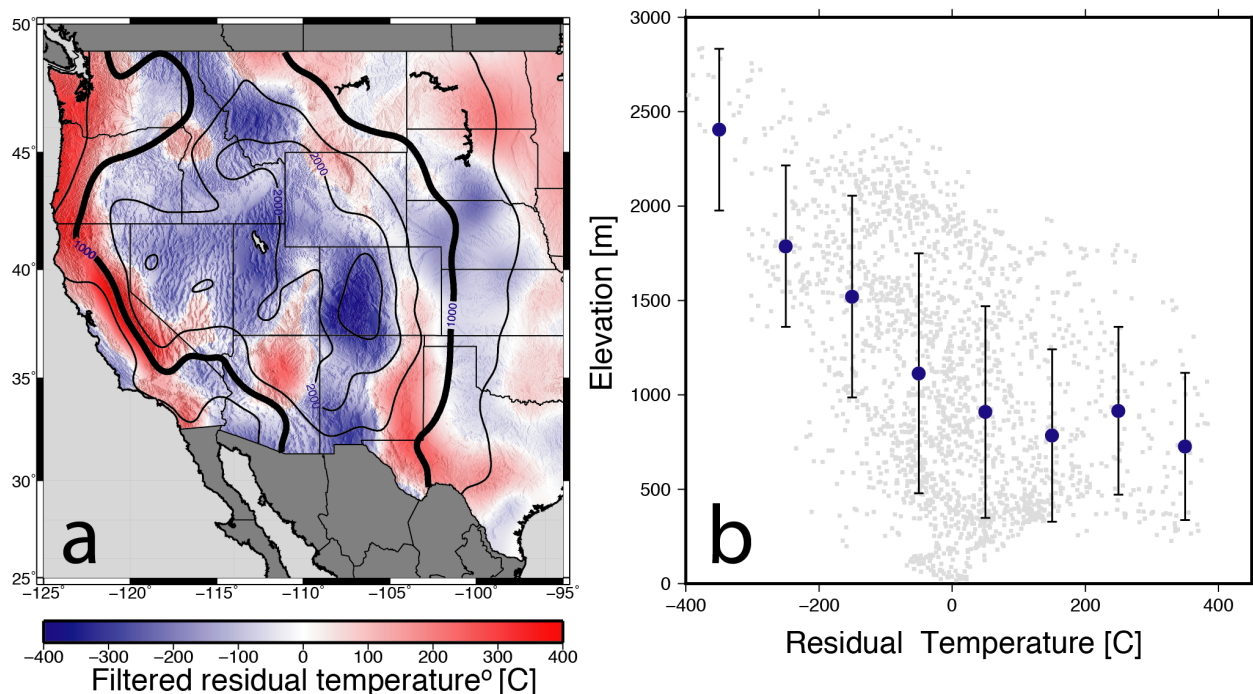
Figure 5. Comparison of residual temperature to elevation. a, Long wavelength residual Moho temperatures overlain by similarly filtered elevation (black contours). **b,** Scatter plot (grey dots) of elevation versus residual temperature. Blue circles are binned averages with 2σ bars.

Figure 5a depicts residual temperatures passed through a 400 km wavelength gaussian filter to eliminate small-scale variations unlikely to contribute to surface elevation, overlain by contours

of Cordilleran elevation similarly filtered to attenuate topography supported by lithospheric strength. A scatter plot compares these smoothed surfaces in Fig. 5b. The Spearman's correlation
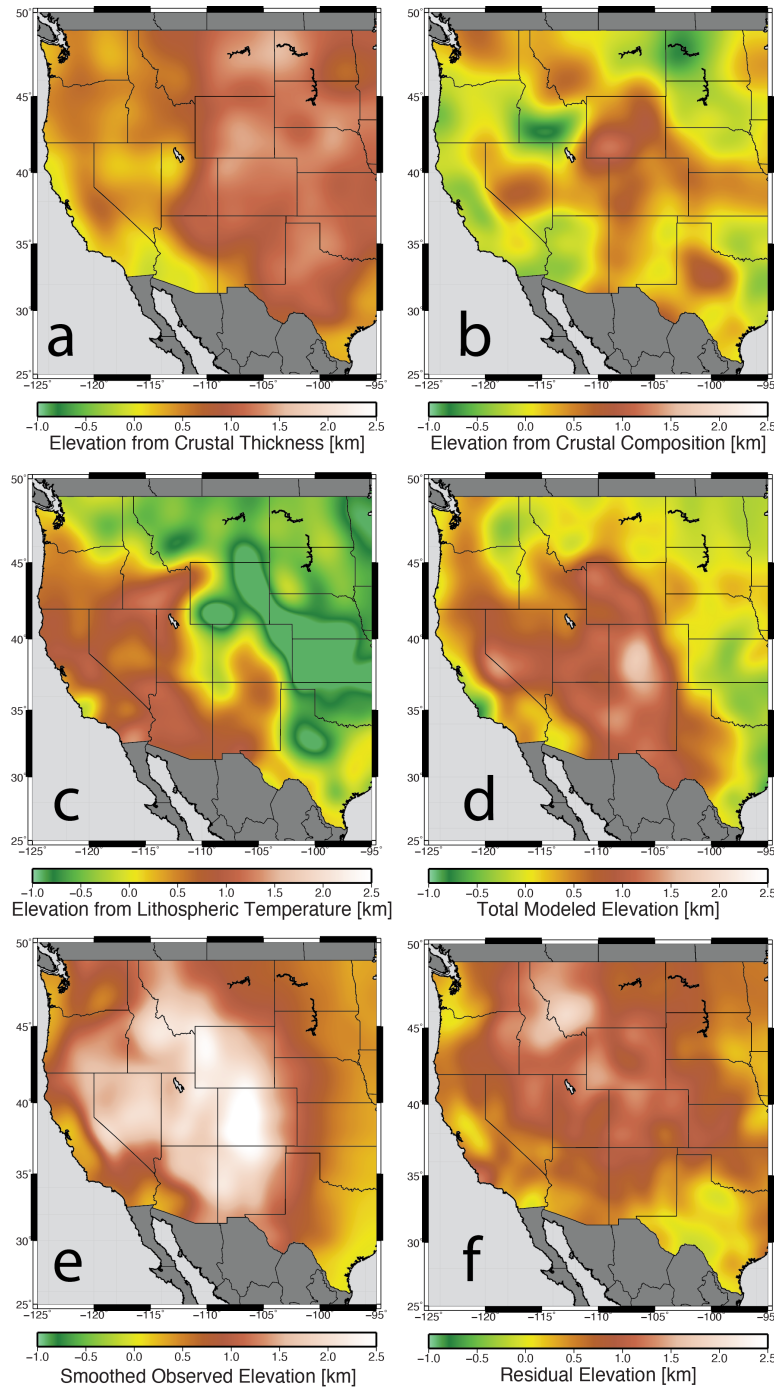
Figure 6. Smoothed elevation contributions from seismically-derived mass fields (after Becker et al. 2014). a, Elevation from crustal thickness variations. **b,** Elevation from crustal compositional mass. **c,** Elevation from lithospheric thermal mass variations. **d,** Total lithospheric model of elevation. **e,** Smoothed observed elevation. **f,** Residual (i.e., asthenospheric-derived) elevation.

coefficient of the relationship (before binned-averaging) is –0.53. A correlation coefficient near zero would indicate no significant relationship, whereas a values near +1 or –1 would require a shared dependence on the same process with little contribution from competing processes. Hence, this correlation coefficient indicates a systematic relationship of greater subsurface buoyancy to uppermost mantle that is colder than the surface heat flow would predict.

To better understand how the discrepancy between surface heat flow and Pn-derived Moho temperature relates to buoyancy responsible for elevation, in section 4.5 we also compare the Gaussian-smoothed residual in Fig. 5a to similarly smoothed models of elevation from the isostatic response to seismic estimates of crustal thickness, crustal density and lithospheric thermal variations (Fig. 6). The Moho temperature residual correlates to elevation modeled from lithospheric buoyancy fields with a Spearman's coefficient of –0.24, while correlation to elevation from asthenospheric buoyancy is –0.44, indicating that buoyancy processes in both the asthenospheric mantle and the lithosphere contribute to the relationship.

4. Discussion

4.1. High Pn-temperature residuals

Most high-temperature residuals in Fig. 1c are found either in relatively stable lithosphere in the eastern third of the study area or in Pacific coastal regions where geotherms are influenced by subduction history. Positive residuals in cratonic North America likely reflect an inappropriate choice of a cooling geotherm where heat transfer has achieved long-term stability. In that case, the cooling geotherm assumed when modeling surface heat flow (red curve in Fig. 3) under-predicts the temperature for a stable lithospheric geotherm (green curve in Fig. 3), resulting in a positive temperature anomaly when subtracted from the Pn observation of Moho temperature. In the forearc of Farallon and Juan de Fuca subduction, slab cooling contributes to anomalously low surface heat flow that underpredicts deep temperatures where slab is no longer present (e.g., Erkan and Blackwell, 2009), but the relatively low Pn velocity (hence high Pn-derived Moho temperature in Fig. 1a) associated with both the past and present subduction is inconsistent with slab-cooling of the upper plate. The most plausible explanation for low Pn velocities there is serpentinization of the Cascadia forearc (Hyndman and Peacock, 2003; Blakely et al., 2005) and Great Valley/Sierra Nevada range, whereas temperature calculations in Schutt et al. (2018) assume a uniform (dry) mantle composition.

4.2. Low Pn-temperature residuals

Deviations from the MM3 spinel lherzolite mantle composition (Baker and Stolper, 1994) assumed by Schutt et al. (2018) cannot explain large negative residual Moho temperatures, as many plausible alternative mantle lithologies favor slower seismic velocities (Schutt et al., 2018). One exception is peridotite, but a plausible 20% melt depletion would increase spinel peridotite v_P by less than 0.5% (Schutt and Lesher, 2006), translating to a 60-80 °C error in temperature for typical low temperatures found in the Cordillera. Discrepancies in Fig. 1c may partially reflect spatial variations in thermal conductivity and radioactive heat production associated with variable crustal composition. However, for plausible changes in these geotherm modeling parameters, changes in estimates of the heat-flow-derived Moho temperature are small relative to the discrepancies in Fig. 1c (Supplementary Materials). Observations of Pn-derived Moho temperature that are hundreds of degrees lower than those modeled from surface heat flow are all-the-more puzzling given that the half-space cooling model adopted here is a low-temperature end-member that systematically underpredicts temperatures for a conductive geotherm in which heat is supplied by asthenospheric convection (Fig. 3). Moreover, a systematic relationship of colder-than-expected lithosphere to higher elevations (Fig. 5) is counter-intuitive.

4.3. Hypothesis testing

4.3.1. Mechanical chilling by flat-slab subduction

Chilling of the lower lithosphere by the Laramide flat-slab subduction episode (Humphreys et al., 2003) suggests one possible explanation for reduced Moho temperature in the western U.S. Cordillera. Cooling of the lithosphere during a flat-slab event, followed by warming and thermal expansion, has been suggested as a possible mechanism for Cenozoic uplift of the Colorado

Plateau (Roy et al., 2009), and the low thermal diffusivity of rock conceivably would permit a residual temperature anomaly to persist to the present day.
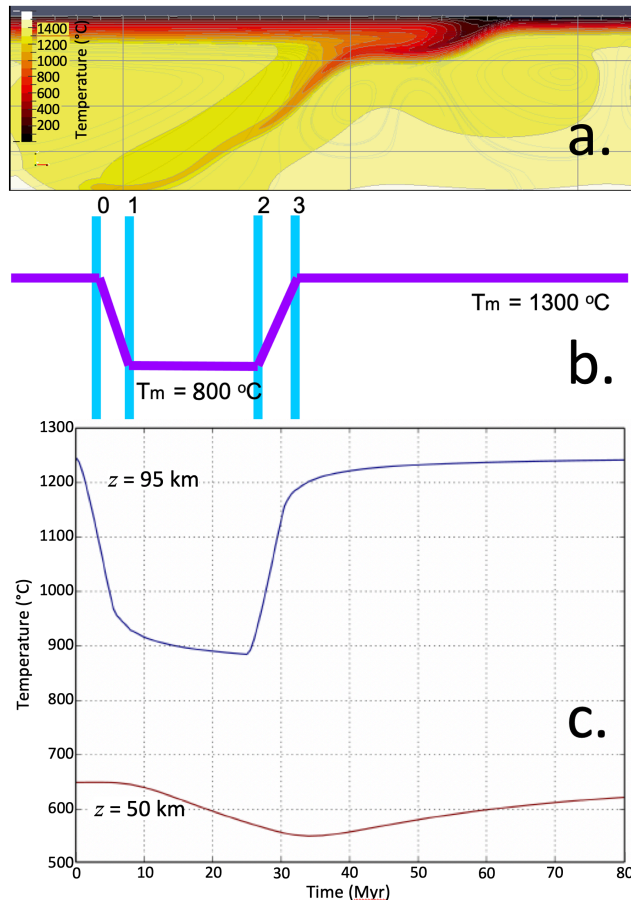
Figure 7. Modeling of transient thermal perturbation by flat slab subduction. a, Cooling of the distal subduction wedge peaks at ~ 800 °C in dynamical models of slab flattening (Kanda et al., 2021). **b,** Basal (200 km) boundary condition approximating temperature history of the western U.S. Cordilleran lithosphere for a transient conductive thermal model invoking slab flattening from 80 (time 0) to 50 Ma (time 3). **c,** Temperature near the base of the lithosphere (blue line) is strongly perturbed coincident with slab flattening but quickly re-equilibrates. Temperature near the Moho (red) is perturbed longer but is only ~ 25 °C cooler than steady-state by 50 Myr after the flat slab event.

Dynamical modeling of processes by which slabs flatten (Kanda et al., 2021) suggests that asthenospheric temperatures in distal regions of flattened slab can drop as low as 800 °C (Fig. 7a). The dynamical model neglects the enthalpy changes associated with hydration discussed in section 4.3.2, so 800 °C can be considered a lower bound on asthenospheric temperatures during flat slab subduction. We use a semi-analytic time-dependent conductive thermal model (described in section 4.3.2) with a basal lithospheric temperature boundary condition that approximates time-history of the Laramide flat slab event (Fig. 7b) to evaluate possible perturbation of the modern-day Moho temperature. Temperatures near the base of the lithosphere react strongly but re-equilibrate quickly, while the Moho temperature responds more slowly, and the perturbation persists longer (Fig. 7c). Nevertheless, by 50 Myr after the flat slab subduction event, the thermal perturbation is only a few tens of degrees and hence much smaller than the several-hundred °C cold anomalies in Cordilleran regions of Fig. 1c. Moreover, the conductive thermal expression of basal chilling of the lithosphere would also be expected to reduce the surface heat flow, with an even greater temporal delay of expression than that at the Moho. The net result of modeling modern Moho temperature from surface heat flow assuming steady-state conduction would thus likely be a warmer, rather than colder, apparent Moho thermal anomaly, suggesting transient thermal effects of Laramide flat slab subduction are an unlikely explanation for observed Moho temperatures that are lower than expected based on such models.

4.3.2. Melt and crustal hydration reaction enthalpy

Thermodynamic modeling of rock reactions in the presence of water (Ma and Lowry, 2017) suggests that hydration of the lower crust consumes garnets into melts that absorb latent

heat, thus reducing lower crustal temperature. Conversely, hydration reactions in the mantle and mid- to upper-crust are exothermic, increasing temperature and adding to heat flow. Following previous modeling (Ma and Lowry, 2017), we use the thermodynamic code Perple_X (Connolly, 2009) to simulate pressure-, temperature-, and chemistry-dependent mineral equations of state for equilibrium mineral assemblages via linear programming minimization of the Gibbs free energy at given entropy and volume. Our models assume crustal chemistries with weight percentage of components for three different major-element chemistries corresponding to averages for the upper, middle and lower crust from Rudnick and Gao (2003), assuming a 15 km thickness for each layer. We use a thermodynamical database (Holland and Powell, 2011) and mineral solution data (Fuhrman and Lindsley, 1988; Holland and Powell, 1996; Holland and Powell, 1998; Dale et al., 2000; Holland and Powell, 2001; Holland and Powell 2003; White et al., 2001) considered most suitable for modeling of hydration reactions by the developer of the software (Guerri et al., 2015). The assumed geothermal gradient approximates equation (3) with the preferred thermal conductivity and crustal heating parameters and a Moho temperature of 730 °C typical of the interior Colorado Plateau. The temperature change associated with hydration reactions can then be calculated from the difference in enthalpy with and without an H_2O constituent present. Hydration results in a complicated perturbational thermal profile for the crust (Fig. 8a). Here, the 0–3 wt-% range modeled for hydration encompasses the range necessary to match observed variations in bulk crustal v_P/v_S and lower crustal density (Ma and Lowry, 2017). Above ~35 km depth, where orthopyroxene and plagioclase dominate the mineral assemblage, hydration reactions are exothermic and raise crustal temperatures by up to 100 °C (depending on P-T conditions and wt-% water). In the garnet-clinopyroxene assemblage at greater depths, however, temperatures decrease by up to 75 °C because latent heat of fusion is absorbed by hydrous melting of garnet.
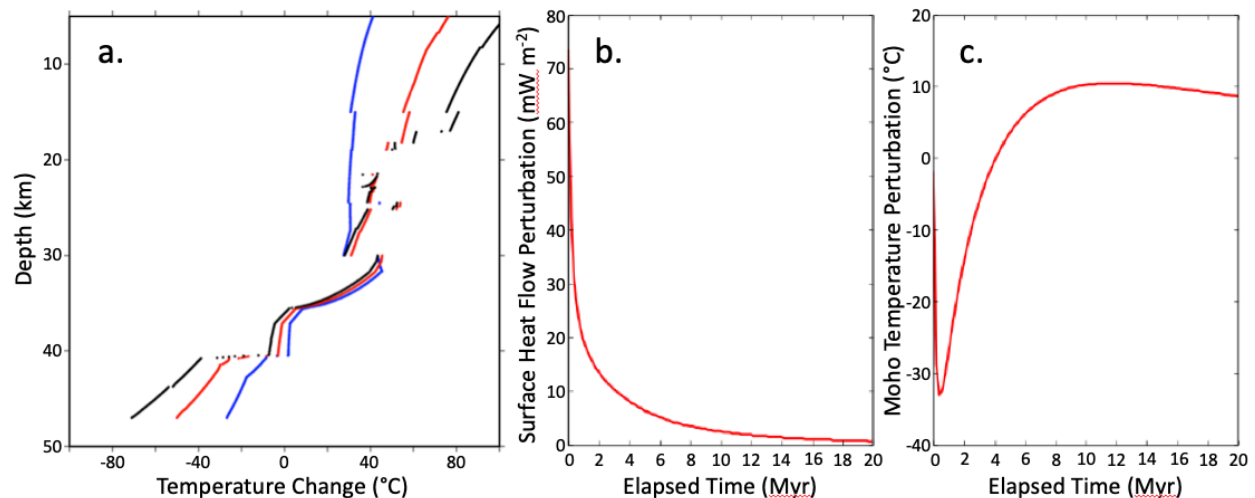
Figure 8. Modeling of transient thermal perturbations by hydration reactions. a, Temperature change with depth in the crust accompanying one (blue), two (red) and three (black) wt-% hydration of the mineral assemblage. **b,** Transient perturbation of surface heat flow by an instantaneous three wt-% hydration event. **c,** Transient perturbation of Moho temperature by a three wt-% hydration event.

Time-dependent modeling of the transient effect of hydration on Moho temperature and surface heat flow (Fig. 8bc) exploits linearity of solutions associated with uniform thermal transfer properties, and thus examines propagation only of the hydration-related temperature perturbation relative to an unperturbed geotherm, $\Delta T = 0$, in a 100 km-thick lithosphere with boundary conditions $\Delta T|_{z=0} = \Delta T|_{z=100\text{ km}} = 0$ °C. We use the one-dimensional heat equation:

$$\kappa \frac{\partial^2 T}{\partial z^2} = \frac{\partial T}{\partial t} + A(z, t) \qquad (5)$$

in which κ is thermal diffusivity (approximated to be 10^{-6}), and A is heat production. Temperature is perturbed at time $t = 0$ (defined to be the time of initial hydration) as:

$$\Delta T(z, t = 0) = \Delta T_1(H\{d_1\} - H\{d_2\}) + \Delta T_2(H\{d_2\} - H\{d_3\}) \qquad (6)$$

where H is the Heaviside function, ΔT_1 is the approximate mean exothermic temperature change from depths $d_1 = 1$ km to $d_2 = 35$ km, and ΔT_2 is the approximate mean endothermic temperature change from depths $d_2 = 35$ km to $d_3 = 45$ km. We assume an instantaneous hydration of the entire crust and examine conductive thermal transfer here because it is the slowest process of heat transfer, giving an upper bound on the time from hydration reaction to an observed change in Moho temperature or surface heat flow. Results of the calculation suggest that a ~ 70 mW m^{-2} perturbation of the surface heat flow (Fig. 8b) is evident immediately and decays slowly on timescales of order 10 Myr, whereas peak reduction of the Moho temperature requires of order 1 Myr and decays quickly, reversing to a temperature increase associated with the net change in heat of the crustal column after ~ 5 Myr.

These results suggest that perturbations inferred in our analyses of the relationship of surface heat flow to Moho temperature should be most robustly evident in the perturbation of surface heat flow and primarily during the first few million years after a hydration event occurs. This calculation is somewhat misleading, however, because it did not include the effects of deeper hydration of the mantle lithosphere and asthenospheric subduction wedge. Hydration of a mantle mineral assemblage is also an exothermic reaction (Peacock, 1987) and would lead to enhanced temperatures and anomalously high surface heat flow maintained over much longer timescales than shown here. Instantaneous transport of water through the column is also an oversimplification, as the hydration currently observed deep in the Cordilleran upper mantle (Meqbel et al., 2014) can be expected to continue to transport upward toward the surface by a combination of diffusion, melt absorption/flux/devolatilization, and convection for a long time to come. On the other hand, advective transfer of heat by melts and volatile constituents moving up the lithospheric column would further amplify surface heat flow on shorter timescales. Given the neglect of many of these transport processes and of contributions from thermodynamical heating of the mantle in modeling for Fig. 8, interpretation of the model should emphasize the relative effects of thermodynamics on heat flow versus on Moho temperature rather than the timescales of thermal perturbations.

Hydration reactions also increase the abundance of crustal quartz (Ma and Lowry, 2017), lowering the seismic velocity ratio (v_P/v_S). Low bulk crustal v_P/v_S is found throughout the Cordilleran region (Lowry and Pérez-Gussinyé, 2011; Ma and Lowry, 2017) where residual Moho temperatures are low in Fig. 1c. Widespread Cordilleran metasomatism and melting is corroborated by other geophysically-inferred distributions of modern-day partial melt and hydration as well. S-wave velocities and electrical conductivity imaging suggest up to 3% partial melt in the lower crust of the Basin and Range and Rio Grande rifts (Wagner et al., 2012; Meqbel et al., 2014). Distributions of lower crustal xenoliths (Jones et al., 2015) and a large Moho density contrast in the western U.S. (Schmandt et al., 2015) also support the inference that Laramide

hydration of the base of Cordilleran lithosphere replaced garnets with less dense mineral phases. Surface wave tomography further suggests that hydration of the lower crust contributed several hundred meters to the elevation of the Colorado Plateau and surrounding regions (Porter et al., 2017).
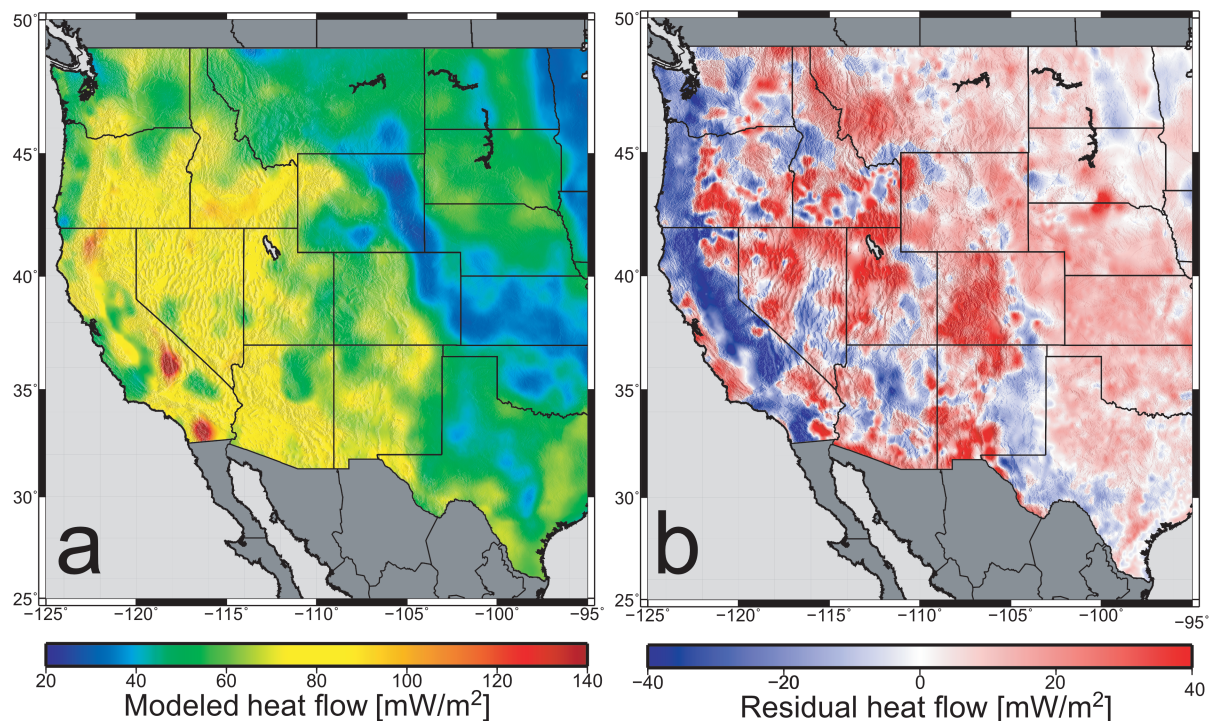
Figure 9. Surface heat flow anomalies. a, Heat flow modeled from Pn measurements of Moho temperature. **b,** Residual heat flow; Observed (see Fig. 2a) minus modeled.

4.4. Modeling surface heat flow from Pn temperature

An alternative way to examine the discrepancy between surface heat flow measurements and estimates of Moho temperature from Pn tomography is to find a steady-state conductive geotherm that matches the measured Moho temperature and calculate the surface heat flow associated with that geotherm by inverting equation (4). Here, we assume the same parameterization of the conductive geotherm used in our preferred modeling of Moho temperature from heat flow (Fig. 1b), including climatic mean surface temperature (Fig. 2d), asthenospheric potential temperature from shear wave velocities at 230 km depth, temperature-dependent thermal conductivity parameters corresponding to mean values for crustal rock measurements, and a uniform exponentially-decreasing crustal heat production profile with $l_{rad} = 14$ km and $A_0 = 2.6$ $\mu W/m^3$. The resulting calculation of surface heat flow (Fig. 9a) is strongly correlative with observed heat flow (Fig. 2a) but has much lower variance. The residual (Fig. 9b, observed minus modeled) exhibits observed heat flow generally higher than modeled throughout the Cordilleran region of high surface elevation, where our conductive thermal modeling of surface heat flow described in earlier sections finds Moho temperatures derived from Pn measurements to be anomalously low.

Thermodynamical modeling of crustal hydration reactions described in the previous section predicts both a lowering of Moho temperature and an increase in surface heat flow lasting of order several million years, but the modeled Moho temperature perturbations (~30 °C in Fig. 8c) are a small fraction of the residual anomalies depicted in Fig. 1c, which exceed 300 °C in some areas. The model prediction of hydration-related transient surface heat flow perturbations (up to ~70 mW m^{-2} in Fig 8b), however, is of the same order (10s of mW/m^2) as those we observe (Fig. 9b). The thermodynamical model in section 4.3.2 neglects the perturbation of surface heat flow expected for advective transfer of heat with vertical migration of the melt and volatile constituents, as well as the contribution of exothermic hydration reactions in the mantle, so hydration- and melt-related heat flow could range even higher and persist for much longer timescales than the model prediction in Fig. 8b. Hence, while both Moho cooling and upper-crustal heating contribute to the discrepancy between surface heat flow and Pn-derived Moho temperature, the "Moho temperature anomaly" discussed in this paper is in fact predominantly a surface heat flow anomaly that, when modeled with a steady-state conductive geotherm, overpredicts the Moho temperature.

4.5. Relating elevation contributions to Moho temperature anomaly

To query the provenance of buoyancy variations responsible for the observed correlation of elevation to the difference in Pn- and surface heat flow-derived temperatures (Fig. 5), we calculate elevations modeled from buoyancy variations associated with crustal thickness (Fig. 6a), crustal composition derived from bulk crustal seismic velocity ratios (Fig. 6b), and lithospheric temperature variation (Fig. 6c) using an approach similar to that of Becker et al. (2014). Here, thermal modeling uses equation (3) to match Pn-derived Moho temperatures, and the crustal thickness and bulk v_P/v_S are estimated from joint inversion of gravity and seismic receiver functions (Lowry and Pérez-Gussinyé, 2011; Ma and Lowry, 2017). The vertical normal stress loads these density variations exert on the lithosphere are flexurally filtered using a uniform 20 km effective elastic thickness. The resulting models of elevation are then smoothed using the same 400 km Gaussian filter applied to observed elevation and the Moho temperature residual in Fig. 5.

Correlations of the Moho temperature residual (Fig. 5a) with elevation models of individual seismically-derived mass fields are generally lower than the (–0.53) correlation of the temperature discrepancy with observed elevation (Fig. 5b). The correlation with elevation derived from crustal thickness (Fig. 6a) is –0.10, with elevation from crustal composition (Fig. 6b) is –0.36, and with elevation from lithospheric temperature (Fig. 6c) is 0.04. Correlation with the total modeled elevation (Fig. 6d) is –0.24, and with the residual (observed minus modeled, Fig. 6f) elevation that Becker et al. (2014) interpreted as resulting from asthenospheric buoyancy is –0.44.

It is not surprising that correlations of the Moho temperature residual (Fig. 5a) with individual constituents of elevation would be somewhat lower than with the total elevation. Correlations of modeled elevations from isolated mass fields with the observed total elevation are 0.17 (crustal thickness), 0.48 (crustal composition), 0.23 (lithospheric temperature), 0.77 (total modeled) and 0.58 (residual). These are conditioned by the relative size of each contribution and the degree of correlation or anticorrelation between mass fields (for example, the crustal thickness

and lithospheric temperature mass fields are strongly anticorrelated and largely offset one another in total elevation).

Model elevation fields that are nearly as correlated with the thermal anomaly (albeit with opposite sign) as they are with total elevation are strong candidates for having been conditioned by the same process(es) responsible for the thermal anomaly. The strongest correlations we observe to the Moho temperature anomalies, with crustal composition and asthenospheric elevation fields, we interpret to be supportive of our primary conclusion that discrepancies in surface heat flow and Moho temperature primarily reflect transient hydration-induced thermodynamical and advective temperature anomalies. Crustal composition predominantly relates to the history of crustal hydration (Ma and Lowry, 2017), while the asthenospheric mass anomalies in Fig. 6f most probably relate to heat released by metasomatism of the back-arc asthenospheric wedge during subduction episodes. Although our thermodynamical modeling to produce Fig. 8 focused entirely on the effects of hydration in the crust, hydration of mantle chemistry is a similarly exothermic reaction. The hydrated asthenosphere is much thicker than the crust, so that added heat may contribute a similar or larger amount to the total elevation as that from the lithospheric mass processes.

5. Conclusions

Accurate estimates of mantle temperature from seismic velocity (Schutt et al., 2018) enable comparisons to steady-state conductive geotherm models of surface heat flow. Discrepancies between these two measurement fields are not explained by plausible spatial variations in crustal thermal conductivity, radioactive heat production, or mantle potential temperature, but must instead invoke time-dependent, advective and/or thermodynamic processes that regionally violate steady-state conduction. Counterintuitively, Cordilleran high elevations are underlain by colder uppermost mantle than predicted by surface heat flow. When elevation is separated into constituent buoyancy contributions, strongest correlations are observed with crustal compositional buoyancy (inferred from bulk crustal v_P/v_S variations) and asthenospheric buoyancy (from residual elevation after lithospheric contributions are removed). The most plausible hypothesis to explain the relationship invokes subduction back-arc hydration that adds heat to the mantle asthenosphere and mid- to upper crust via hydration reactions, while consuming lower-crustal garnet into melts. In this hypothesis, the geotherm discrepancy reflects slight cooling of the lower crust and uppermost mantle by absorption of latent heat into melting, and large amplification of the surface heat flow by advective transport of heat with melts and volatile flux, plus additional heat-release by hydration reactions in the mid-crust and asthenospheric mantle. This hypothesis also explains why subduction back-arcs globally exhibit long-lived signatures of high surface heat flow and asthenospheric buoyancy, despite refrigeration of wedge flow by circulation over a warming subducted slab. The potential role of hydration and volatile flux in asthenospheric heating and lithospheric thermal transfer has been relatively under-explored in geodynamical modeling studies, but the software innovations needed to address this are becoming available. Consequently, we anticipate that dynamical models addressing the thermodynamical role of volatile transport in orogeny will be a fruitful future enterprise.

References

Artemieva, I.M., Mooney, W.D., 2001. Thermal thickness and evolution of Precambrian lithosphere: A global study. J. Geophys. Res. 106, 16387–16414. https://doi.org/10.1029/2000JB900439.

Baker, M.B., Stolper, E.M., 1994. Determining the composition of high-pressure mantle melts using diamond aggregates. Geochimica et Cosmochimica Acta 58, 2811–2827. https://doi.org/10.1016/0016-7037(94)90116-3.

Becker, T.W., Faccenna, C., Humphreys, E.D., Lowry, A.R., Miller, M.S., 2014. Static and dynamic support of western United States topography. Earth Planet. Sci. Lett. 402, 234–246. https://doi.org/10.1016/J.EPSL.2013.10.012.

Blackwell, D.D., Negraru, P.T., Richards, M.C., 2007. Assessment of the Enhanced Geothermal System Resource Base of the United States. Nat. Resour. Res. 15, 283–308. https://doi.org/10.1007/s11053-007-9028-7.

Blakely, R.J., Brocher, T.M., Wells, R.E., 2005. Subduction-zone magnetic anomalies and implications for hydrated forearc mantle. Geology 33, 445-448. https://doi.org/10.1130/G21447.1.

Buehler, J.S., Shearer, P.M., 2017. Uppermost mantle seismic velocity structure beneath USArray. J. Geophys. Res. 122, 436–448. https://doi.org/10.1002/2016JB013265.

Cammarano, F., Goes, S., Vacher, P., Giardini, D., 2003. Inferring upper-mantle temperatures from seismic velocities. Phys. Earth Planet. Int. 138, 197–222. https://doi.org/10.1016/S0031-9201(03)00156-0.

Currie, C.A., Hyndman, R.D., 2006. The thermal structure of subduction zone back arcs. J. Geophys. Res. 111. https://doi.org/10.1029/2005JB004024.

Connolly, J.A.D., 2009. The geodynamic equation of state: what and how. Geochem. Geophys. Geosys. 10. https://doi.org/10.1029/2009GC002540.

Dale,J., Holland,T., Powell,R., 2000, Hornblende-garnet-plagioclase thermobarometry: a natural assemblage calibration of the thermodynamics of hornblende. Contributions to Mineralogy and Petrology 140:353-62. https://doi.org/10.1007/s004100000187.

Erkan, K., Blackwell, D., 2009. Transient thermal regimes in the Sierra Nevada and Baja California extinct outer arcs following the cessation of Farallon subduction. J. Geophys. Res. 114. https://doi.org/10.1029/2007JB005498.

Fuhrman, M.L.,Lindsley, D.H., 1988, Ternary-Feldspar Modeling and Thermometry. American Mineralogist 73:201-15.

Furlong, K.P., Chapman, D.S., 2013. Heat Flow, Heat generation, and the thermal state of the lithosphere. Ann. Rev. Earth Planet. Sci. 41, 385–410. https://doi.org/10.1146/annurev.earth.031208.100051.

Gosnold, W.D., 1985. Heat flow and ground water flow in the Great Plains of the United States. J. Geodyn. 4, 247–264. https://doi.org/10.1016/0264-3707(85)90063-8.

Grieser, J., Gommes, R., Cofield, S., Bernardi, M., 2006. Data sources for FAO worldmaps of Koeppen climatologies and climatic net primary production. The Agromet Group, SDRN,

Food and Agriculture Organization of the United Nations, Rome, Italy.

Guerri, M., Cammarano, F., Connolly, J. A., 2015. Effects of chemical composition, water and temperature on physical properties of continental crust. Geochem. Geophys. Geosys. 16, 2431-2449. https://doi.org/10.1002/2015GC005819.

Hacker, B.R., Kelemen, P.B., Behn, M.D., 2015. Continental lower crust. Ann. Rev. Earth Planet. Sci. 43, 167–205. https://doi.org/10.1146/annurev-earth-050212-124117.

Hasterok, D., Gard, M., Webb, J., 2018. On the radiogenic heat production of metamorphic, igneous, and sedimentary rocks. Geosci. Front. 9, 1777–1794. https://doi.org/10.1016/j.gsf.2017.10.012.

Holland, T., Powell, R., 1996. Thermodynamics of order-disorder in minerals: II. Symmetric formalism applied to solid solutions. Am. Mineral. 81, 1425–1437. https://doi.org/10.2138/am-1996-11-1215.

Holland, T., Powell, R., 1998. An internally consistent thermodynamic data set for phases of petrological interest. J. Metamorph. Geol. 16, 309–343. https://doi.org/10.1111/j.1525-1314.1998.00140.x

Holland, T., Powell, R., 2001. Calculation of phase relations involving haplogranitic melts using an internally consistent thermodynamic dataset. J. Petrol. 42, 673–683. https://doi.org/10.1093/petrology/42.4.673

Holland, T., Powell, R., 2003. Activity–composition relations for phases in petrological calculations: an asymmetric multicomponent formulation. Contrib. Mineral. Petrol. 145, 492–501. https://doi.org/10.1007/s00410-003-0464-z.

Huang, Y., Chubakov, V., Mantovani, F., Rudnick, R.L., McDonough, W.F., 2013. A reference Earth model for the heat-producing elements and associated geoneutrino flux. Geochem. Geophys. Geosys. 14, 2003–2029. https://doi.org/10.1002/ggge.20129.

Humphreys, E.D., Hessler, E., Dueker, K., Farmer, G.L., Erslev, E., Atwater, T., 2003. How Laramide-age hydration of North American lithosphere by the Farallon slab controlled subsequent activity in the western United States. Int. Geol. Rev. 45, 575–595. https://doi.org/10.2747/0020-6814.45.7.575.

Hyndman, R. D., Peacock, S. M., 2003. Serpentinization of the forearc mantle. Earth Planet. Sci. Lett. 212, 417-432. https://doi.org/10.1016/S0012-821X(03)00263-2.

Hyndman, R. D., Currie, C. A., Mazzotti, S. P., 2005. Subduction zone backarcs, mobile belts, and orogenic heat. GSA Today 15, 4-10. https://doi.org/10:1130/1052-5173(2005)015<4:SZBMBA>2.0.CO;2.

Jones, C.H., Mahan, K.H., Butcher, L.A., Levandowski, W.B., Farmer, G.L., 2015. Continental uplift through crustal hydration. Geology 43, 355–358. https://doi.org/10.1130/G36509.1.

Kanda, R. V. S., Lowry, A. R., Buiter, S. J. H., 2021. Mounting wedge corner suction driven by lower mantle resistance triggers flattening of subducting slabs. Geochem., Geophys. Geosys. in preparation.

Kukkonen, I.T.T., Jokinen, J., Seipold, U., 1999. Temperature and pressure dependencies of thermal transport properties of rocks: Implications for uncertainties in thermal lithosphere

models and new laboratory measurements of high-grade rocks in the central Fennoscandian shield. Surv. Geophys. 20, 33–59. https://doi.org/10.1023/A:1006655023894.

Lee, C.T.A., Morton, D.M., Kistler, R.W., Baird, A.K., 2007. Petrology and tectonics of Phanerozoic continent formation: From island arcs to accretion and continental arc magmatism. Earth Planet. Sci. Lett. 263, 370–387. https://doi.org/10.1016/j.epsl.2007.09.025.

Lowry, A.R., Pérez-Gussinyé, M., 2011. The role of crustal quartz in controlling Cordilleran deformation. Nature 471, 353–357. https://doi.org/10.1038/nature09912.

Lowry, A.R., Ribe, N.M., Smith, R.B., 2000. Dynamic elevation of the Cordillera, western United States. J. Geophys. Res. 105, 23371–23390. https://doi.org/10.1029/2000JB900182.

Ma, X., Lowry, A.R., 2017. USArray imaging of continental crust in the conterminous United States. Tectonics 36, 2882–2902. https://doi.org/10.1002/2017TC004540.

Mareschal, J., Cunningham, J.P., Lowell, R.P., 1985. Downward continuation of heat flow data: Method and examples from the western United States. Geophysics 50, 846–851. https://doi.org/10.1190/1.1441960.

Meqbel, N.M., Egbert, G.D., Wannamaker, P.E., Kelbert, A., Schultz, A., 2014. Deep electrical resistivity structure of the northwestern U.S. derived from 3-D inversion of USArray magnetotelluric data. Earth Planet. Sci. Lett. 402, 290–304. https://doi.org/10.1016/j.epsl.2013.12.026.

Morgan, P., Sass, J. H., Duffield, W., 2010. Geothermal Resources Evaluation Program of the Eastern San Francisco Volcanic Field, Arizona. Dept. Of Energy Report.

Peacock, S.M., 1987. Thermal effects of metamorphic fluids in subduction zones. Geology 15, 1057-1060. https://doi.org/10.1130/0091-7613(1987)15<1057:TEOMFI>2.0.CO;2.

Pollack, H.N., Chapman, D.S., 1977. On the regional variation of heat flow, geotherms, and lithospheric thickness. Tectonophysics 38, 279–296. https://doi.org/10.1016/0040-1951(77)90215-3.

Porter, R., Hoisch, T., Holt, W.E., 2017. The role of lower-crustal hydration in the tectonic evolution of the Colorado Plateau. Tectonophysics 712–713, 221–231. https://doi.org/10.1016/J.TECTO.2017.05.025.

Roy, M., Jordan, T.H., Pederson, J., 2009. Colorado Plateau magmatism and uplift by warming of heterogeneous lithosphere. Nature 459, 978-982. https://doi.org/10.1038/nature08052.

Rudnick, R.L., Gao, S., 2003. Composition of the Continental Crust, *in* Treatise on Geochemistry, Elsevier.

Schmandt, B., Lin, F.-C., 2014. P and S wave tomography of the mantle beneath the United States. Geophys. Res. Lett. 41, 6342–6349. https://doi.org/10.1002/2014GL061231.

Schmandt, B., Lin, F.-C., Karlstrom, K.E., 2015. Distinct crustal isostasy trends east and west of the Rocky Mountain Front. Geophys. Res. Lett. 42, 10,290-10,298. https://doi.org/10.1002/2015GL066593.

Schutt, D.L., Lowry, A.R., Buehler, J.S., 2018. Moho temperature and mobility of lower crust in the western United States. Geology 46, 219-222. https://doi.org/10.1130/G39507.1.

Schutt, D.L., Lesher, C. E., 2006. Effects of melt depletion on the density and seismic velocity of garnet and spinel lherzolite. J. Geophys. Res. 111. https://doi.org/10.1029/2003JB002950.

Seipold, U., 1998. Temperature dependence of thermal transport properties of crystalline rocks—a general law. Tectonophysics 291, 161-171. https://doi.org/10.1016/S0040-1951(98)00037-7.

Turcotte, D.L., Oxburgh, E.R., 1972. Statistical thermodynamic model for the distribution of crustal heat sources. Science 176, 1021-1022. https://doi.org/10.1126/science.176.4038.1021.

Wagner, L.S., Fouch, M.J., James, D.E., Hanson-Hedgecock, S., 2012. Crust and upper mantle structure beneath the Pacific Northwest from joint inversions of ambient noise and earthquake data. Geochem. Geophys. Geosys. 13. https://doi.org/10.1029/2012GC004353.

White, R.W., Powell, R., Holland, T.J.B., 2001. Calculation of partial melting equilibria in the system Na_2O–CaO–K_2O–FeO–MgO–Al_2O_3–SiO_2–H_2O (NCKFMASH). J. Metamorph. Geol. 19, 139–153. https://doi.org/10.1046/j.0263-4929.2000.00303.x.

Zhou, Q., Liu, L., Hu, J., 2018. Western US volcanism due to intruding oceanic mantle driven by ancient Farallon slabs. Nat. Geosci. 11, 70-76. https://doi.org/10.1038/s41561-017-0035-y.

Data and code availability: Code for conductive geotherm modeling and data including heat flow, Pn-derived Moho temperatures, and crustal thickness is available at https://github.com/mberry28/conductive_geotherm_modeling.

Correspondence and requests for materials should be addressed to Michael A. Berry (michaelberry@tuta.io) or Anthony R. Lowry (tony.lowry@usu.edu).

Supplementary Information

Some of the fields required for conductive thermal modeling of the lithosphere are not straightforward to measure directly. These include variations in the (quartz-sensitive) *A* and *B* parameters of crustal thermal conductivity, three-dimensional distributions of radioactive elements, and potential temperature of the deep upper mantle. We explore the parameter spaces for these more thoroughly in this supplement by trying several different approaches for each, and we assess the potential for variations in these properties to explain discrepancies in temperature structures inferred from Pn-derived Moho temperature and surface heat flow (Fig. 5).

Asthenospheric Mantle Potential Temperature

We examined several different approaches to specifying mantle asthenospheric potential temperature, including using a uniform expected value everywhere, solving for a spatially-varying
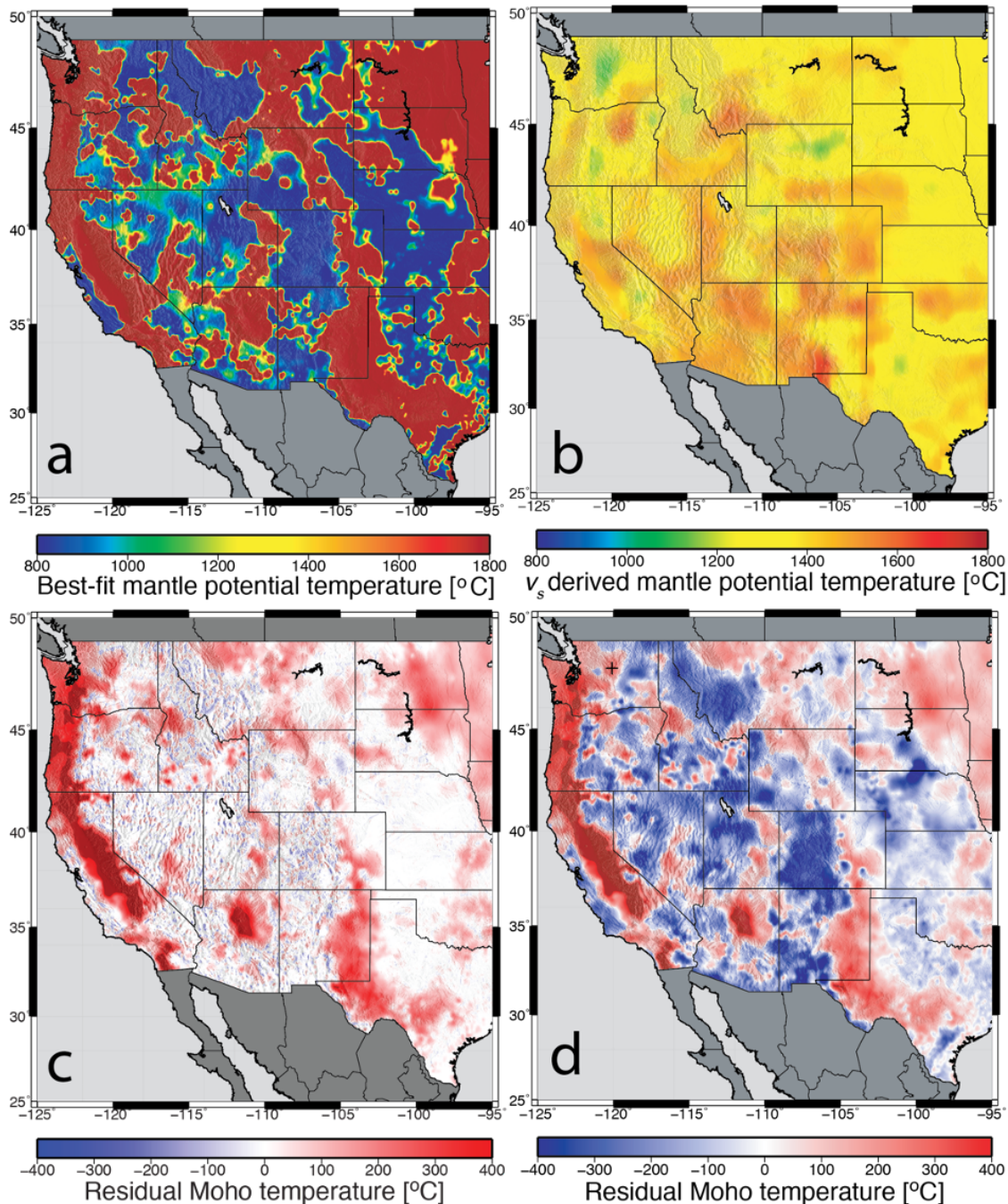
Figure S1. Alternative approaches to estimating mantle asthenospheric potential temperature. a, Asthenospheric temperature (in the range 400–2200 °C) that minimizes differences between Pn- and surface heat flow-derived Moho temperature estimates. **b,** Asthenospheric temperature from mineral physics mapping (Cammarano et al., 2003) of deep tomographic shear velocity (Schmandt and Lin, 2014) to temperature. **c,** Residual Moho temperature using asthenospheric mantle temperature in a. **d,** Residual Moho temperature using asthenospheric mantle temperature in b.

temperature that minimized the misfit between the heat flow- and Pn-derived estimates of Moho temperatures, and specifying a spatially-varying asthenospheric temperature based on mineral physics mapping of tomographic mantle shear wave velocity to temperature variations. Solving for the spatially-varying mantle potential temperature that minimizes misfit substantially reduces the geotherm discrepancies if temperatures are permitted to vary in a large range, but the resulting

estimates of asthenospheric temperatures exceed 1800 °C for roughly half of the map space (Fig. S1a). Counterintuitively, the highest resulting estimates of asthenospheric temperature are in those regions where Pn-derived estimates of Moho temperature are anomalously low (Schutt et al., 2018). Inspection of the estimation procedure reveals that, where Moho temperature is unusually low, the algorithm matches those temperatures by imposing a larger conductive thermal length-scale l_{con}, but it offsets the resulting reduction of surface heat flow by also imposing a higher asthenospheric temperature. In effect, it forces a match to both data sets by increasing both the thickness and the temperature differential across the thermal boundary layer.

The estimates of asthenospheric temperature from minimization of the difference in Pn-derived and surface heat flow-derived Moho temperature (Fig. S1a) are not only much more variable than could reasonably be expected in a convecting mantle, they are also vastly inconsistent with the temperature variations suggested by seismic velocities at asthenospheric depths. Fig. S1b shows tomographic shear wave velocities (Schmandt and Lin, 2014) at a depth of 230 km converted to temperature via a widely-used mineral-physics relation (Cammarano et al., 2003), assuming a mean mantle potential temperature of 1410 °C (Sarafian et al., 2017). This approach results in much larger misfits in Moho temperature estimates (compare Fig. S1cd) but has the advantage of being physically plausible and consistent with observed mantle physical properties. We interpret the highly-variable asthenospheric temperatures in Fig. S1a to be artefacts introduced by violation of the conductive thermophysics assumed by the surface heat flow model of the geotherm, and hence we use the asthenospheric temperature variation in Fig. S1b and 2c as the basis for analyses depicted in Fig. 1bc and the conclusions drawn therefrom.

The RMS of misfit in Moho temperature estimates shown in Fig. S1d is 198.8 °C. We also examined misfit for the simpler case of a uniform (1410 °C) mantle potential temperature and found RMS misfit to be slightly smaller (195.4 °C), albeit with a negligibly different pattern of spatial variation in the resulting residual.
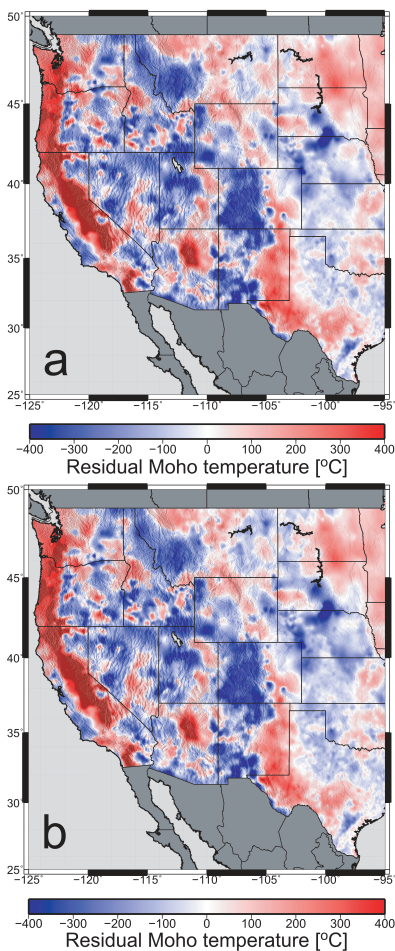
Conductivity Parameters

Rock thermal conductivity, k, empirically depends upon temperature, T [°K], and rock composition as $k = 1/(A + BT)$ (Siepold, 1998), where A and B are lithology-dependent (and sensitive primarily to the presence of quartz in crustal rocks; Kukkonen et al., 1999). Quartz abundance is highly variable in continental crust (Ma and Lowry, 2017; Lowry and Pérez-Gussinyé, 2011), implying that A and B are similarly variable. Hence, we examine three different approaches to specifying these parameters in the crust including a uniform parameterization that minimizes misfit between the Pn- and heat flow-derived estimates of Moho temperature, a uniform parameterization corresponding to the mean of measurements for crustal rocks, and a laterally-varying parameterization informed by bulk-crustal seismic velocity ratios, which are also quartz-sensitive.

For the minimization problem, we calculated RMS misfit in Moho temperature estimates for a broad range of combinations of A and B encompassing the range of measurements for crustal rocks (Fig. 4a). A region of the parameter-space with misfits ~200 °C trends through the axis of the measurements for crustal rocks (Kukkonen et al., 1999; Seipold, 1998). Our best fitting parameter is $A = 0.28$ and $B = 3.1 \times 10^{-4}$, while the mean of lab measurements for crustal rocks from Seipold (1998) is $A = 0.28$ and $B = 3.2 \times 10^{-4}$.

Seismic velocity ratios, v_P/v_S, are sensitive to quartz content and can be estimated from seismic inversion (Ma and Lowry, 2017; Lowry and Pérez-Gussinyé, 2011), so we also examined whether v_P/v_S might be useful as a proxy for lateral variations in crustal lithology. We first assumed that crustal thermal conductivity parameters would fall on a trend between granite ($A = 0.20$, $B = 4.1 \times 10^{-4}$) and basalt ($A = 0.36$, $B = 1.4 \times 10^{-4}$). We further assumed that the mean crustal v_P/v_S would

correspond to a mean thermal lithology midway between those two endpoints, and we examined how the misfit in Pn- versus heat flow-derived estimates of Moho temperature depended on a scaling parameter varied from zero (i.e., with A and B independent of v_P/v_S) to one (in which the minimum v_P/v_S was assigned conductivity parameters for granite, and the maximum for basalt, with conductivity parameters linearly scaled to intermediate v_P/v_S). This approach produced a small increase in RMS misfit from the lithology-independent case (200.5 °C) to a full scaling of lithology using v_P/v_S as a proxy (201.2 °C). Consequently, we use a uniform crustal parameterization with mean measurements of parameters for crustal rocks in the results shown in Figs. 1 and 5. The residual Moho temperatures using seismic velocity ratios as a proxy for laterally-varying crustal lithology are shown in Fig. S2b.


Figure S2. Residual Moho temperatures for various approaches to representing crustal conductivity structure. a, Residual Moho temperature for uniform crustal thermal conductivity parameters corresponding to the mean of laboratory measurements for crustal rocks. **b**, Residual Moho temperature using conductivity parameters linearly scaled to basalt and granitic end-member values implicit in bulk crustal v_P/v_S.

Mantle thermal conductivity plays relatively little role in our analysis, both because the "Moho temperature" is calculated only three km below the top of the mantle (at the putative centroid of the Fresnel kernel for Pn) and because the B parameter for mantle rocks changes the conductivity negligibly for most of the range of temperatures of the Pn temperature product. Hence, we use a constant (2.2 W m^{-1} °K^{-1}) thermal conductivity to represent the mantle.

Radioactive Heat Production

Radioactive heating influences both the temperature gradient and the crustal contribution to total surface heat flow, Q_r (which thus determines also the remainder mantle contribution to surface heat flow that defines thickness of the thermal boundary layer). There are several equally plausible models used to describe the depth distribution of crustal heat production, $A(z)$, within the crust (Furlong and Chapman, 2013), all of which generally require higher heat production in the shallow crystalline crust and lower production in the lower crust consistent with the melt-affinity of radioactive elements, petrologic constraints on crustal composition (Hacker et al., 2015; Huang et al., 2013; Rudnick and Gao, 2003; Lee et al., 2007), and $Q_r < Q_S$ dictates lower heat production deeper in the crust than we measure at the surface (Lachenbruch, 1970). We follow Lachenbruch (1970) in assuming an exponential decrease in heat production with depth, parameterized by a surface heat production A_0 [μW/m^3] and length-scale l_{rad} [km].

Initially, we parameterized surface heat production using aerospectral gamma measurements (Duval et al., 2005; Kucks and Hill, 2005). Although the measurements reflect isotope decay only in the upper half-meter or so of the soil, earlier analyses (Lowry and Pérez-Gussinyé, 2011) postulated that surficial sediments might partially reflect weathering of underlying basement and thus improve upon analyses that neglect these observations. However,
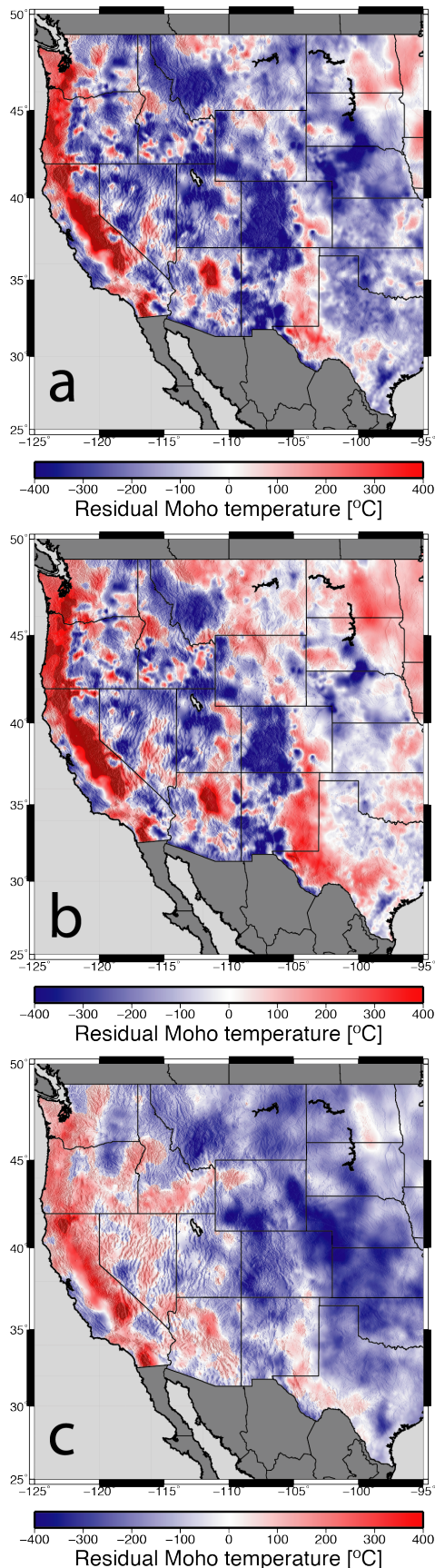
our analyses found that a broad range of uniform choices for A_0 yielded lower RMS misfit between Pn- versus heat flow-derived Moho temperatures than models that used spatially-varying A_0 based on aerospectral gamma data. For this reason, our preferred model described in Figs. 1 and 5 used uniform parameters for surface and depth scaling of heat production. However, the Moho temperature residuals obtained with and without spatially varying surface heat production are very similar (compare, e.g., Fig. S3a with Fig. S3b).

Figure S3. Residual Moho temperatures for representative models of crustal heat production. a, Moho temperature model using spatially varying surface heat production, A_0, derived from aerospectral gamma measurements (Duval et al., 2005). **b,** Model using the uniform crustal heating model that minimized RMS misfit of Moho temperatures (i.e., identical to Fig. 1c). **c,** Model using the uniform crustal heating model that yields a secondary minimum in RMS misfit in Fig. 4b (l_{rad} = 50 km, A_0 = 0.75 µW/m³).

RMS misfit of the Moho temperature estimates for a broad range of uniform choices of l_{rad} and A_0 are shown in Fig. 4b. Most choices of radioactive heating parameters will generate crustal contributions to surface heat flow Q_r that exceed measured heat flow Q_S in some regions where heat flow is anomalously low (such as for example the northern Sierra Nevada range and Cascadia forearc; Fig. 2b), and the highest values of A_0 and/or l_{rad} yield $Q_r > Q_S + Q_m$ (for a reasonable expectation of minimum mantle heat flux, Q_m = 18 mW/m²) nearly everywhere on the map. The calculation used to produce Fig. 4b addressed this problem by reducing both A_0 and l_{rad} by 1% at those specific locations where $Q_r + Q_m > Q_S$ (and repeated the operation at those locations until they achieved $Q_r + Q_m < Q_S$). The percentage of the map with reduced Q_r is indicated by color saturation in Fig. 4b, with white corresponding to reduced Q_r for the entire map. As noted in the main manuscript, misfit in the Moho temperature estimates was minimized by l_{rad} = 17 km and A_0 = 2.6 µW/m³, consistent with expectations derived from petrologic models of average continental crust (Rudnick and Gao, 2003; Lee et al., 2007; Huang et al., 2013) and an exposed crustal cross-section of the North American Cordillera (Hacker et al., 2015) (Fig. 4b). The minimum-residual uniform crustal heating parameters were used in our preferred model (Figs. 1 and 5) and the corresponding map of residual Moho temperature is repeated in Fig. S3b. A secondary minimum was observed for l_{rad} = 50 km and A_0 = 0.7 mW/m³, and while this combination is considered a petrologically unlikely representation of continental crust,

it nevertheless yields a residual Moho temperature map that is not substantively different than that produced by other parameterizations of the conductive geotherm (Fig. S3c).
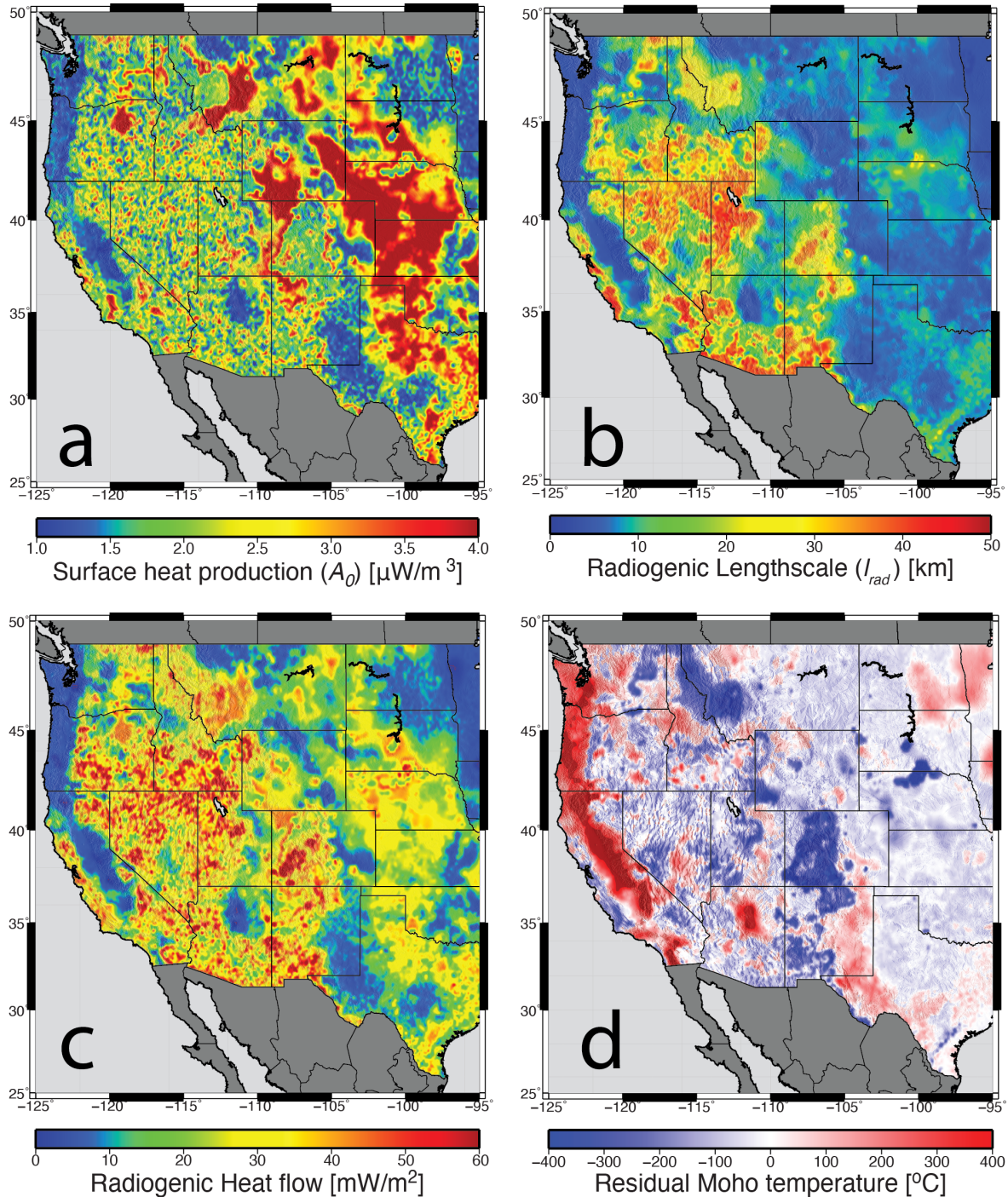

Figure S4. Spatially-varying crustal radioactive heating model that minimizes Moho temperature misfit. a, Surface heat production parameter A_0. **b,** Radioactive length parameter l_{rad}. **c,** Contribution of crustal radioactive heating to surface heat flow, Q_r, for the model. **d,** Residual Moho temperature anomalies using heat production parameters that best fit Moho temperature.

For completeness, we also solve via grid-search for a spatially varying parameterization of both A_0 and l_{rad} that minimizes the misfit at every location on the map space (Fig. S4). As one

might expect, the RMS misfit of Moho temperature is significantly reduced by tailoring the radioactive heating profile in this manner (from an RMS misfit of 199 °C to 165 °C), but the discrepancies do not disappear entirely (Fig. S4d), and they exhibit a spatial pattern similar to that of the preferred (uniform crustal heating) model (Fig. 1c). Quantitative comparison of the Moho temperature anomalies to elevation also yields a similar, if slightly smaller, correlation coefficient (–0.46 versus –0.53).

The spatially varying estimates of surface heat production (Fig. S4a) exhibit no clear correlation to independent observations such as aerospectral gamma measurements (Lowry and Pérez-Gussinyé, 2011) or surface geology, except that oceanic-derived crustal blocks along the Pacific coast have low A_0. The radioactive length-scale estimates (Fig. S4b), however, are plausible in that they correlate strongly with estimates of lower-crustal v_P/v_S (Ma and Lowry, 2021), and the sign of the correlation is consistent with the expectation that more granitic rocks should have higher radioactive element concentrations owing to affinity of those elements to melts. However, there are several reasons to be skeptical that the spatially varying parameters realistically represent crustal heating variations. Fig. S4c shows the model's prediction of crustal heating contribution to total surface heat flow, and one problem is that some of the calculated Q_r variations appear to be artefacts related to known transients, advective heat transfer and hydrologic flow anomalies (e.g., in the Cascadia forearc, Cascade volcanoes, and Yellowstone hotspot track). Moreover, the crustal heat production is correlated with high elevation of the Farallon subducted back-arc. We can think of no mechanism by which subduction history would increase bulk-crustal radioactive element concentrations by a factor of two to three as implicit in the map of Q_r, and there is no evidence that ancient subduction back-arcs, such as the Iapetus back-arc stretching from the Caledonian arc across the Appalachian, Illinois and Michigan basins, have enhanced bulk-crustal radioactivity concentrations. One can make a stronger case instead that the distribution of low-temperature Moho anomalies in the Cordillera is localized to regions where lower-crustal melting is expected based on other geophysical observations (Porter et al., 2017; Wagner et al., 2012, Meqbel et al., 2014). For these reasons, we have chosen to use the best-fitting uniform crustal heating model as our preferred solution.
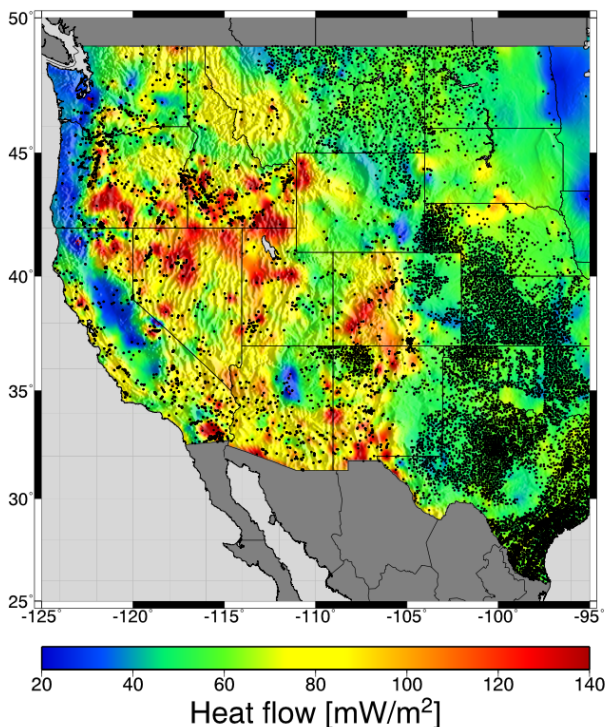
Figure S5. Distribution of borehole surface heat flow measurements. Data from Blackwell et al. (2011) measurements mostly come from bottom hole temperatures in oil and gas wells, with about 10% deriving from temperature profiles for geothermal or academic studies. Sampling is plotted on the filtered heat flow distribution map (Fig. 2a).

Additional References

Duval, J.S., Carson, J.M., Holman, P.B., Darnley, A.G., 2005. Terrestrial radioactivity and gamma-ray exposure in the United States and Canada. U.S. Geol. Surv. Open File Rep. 2005-1413. https://pubs.usgs.gov/of/2005/1413/.

Kucks, R.P., Hill, P.L., 2005. Missouri aeromagnetic and gravity maps and data: a web site for distribution of data. https://doi.org/10.3133/ds128.

Lachenbruch, A.H., 1970. Crustal temperature and heat production: Implications of the linear heat-flow relation. J. Geophys. Res. 75, 3291–3300. https://doi.org/10.1029/JB075i017p03291.

Ma, X., Lowry, A.R., 2021. A two-layer model of continental crust in the conterminous United States. J. Geophys. Res., submitted.

Sarafian, E., Gaetani, G.A., Hauri, E.H., Sarafian, A.R., 2017. Experimental constraints on the damp peridotite solidus and oceanic mantle potential temperature. Science 355 942–945. https://doi.org/10.1126/science.aaj2165.